Journal of Materials Research and Technology 41 (2026) 4844–4853

Contents lists available at ScienceDirect

Journal of Materials Research and Technology

journal homepage: www.elsevier.com/locate/jmrt

# Fabrication of iron-based multiporous structures by combining in-situ reduction with sintering

Isadora Deschamps [a], Daniel A. Schaefer [a], Irene C.M. Mocellin [a], Dmitry Sergeev [b], Mohammed Bouzbib [b], Aloisio N. Klein [a], Tatiana Bendo [a], Kaline P. Furlan [c,*]

[a] Materials Laboratory (LABMAT), Mechanical Engineering Dept – Federal University of Santa Catarina, Brazil
[b] NETZSCH-Gerätebau GmbH, Selb, D-95100, Germany
[c] Karlsruhe Institute of Technology, Institute for Applied Materials, Ceramic Materials and Technologies, Karlsruhe, Germany

ARTICLE INFO

*Keywords:*
Porous iron-based materials
In-situ reduction
Space holder
Powder metallurgy
Sintering

ABSTRACT

Porous iron-based materials are attractive for structural, acoustic, and thermal management applications due to their low cost, availability, and tunable performance. This study introduces a simple and cost-effective route for fabricating multiporous iron structures by combining in-situ reduction and sintering of hematite ($Fe_2O_3$) powders with graphite as space holder. The approach integrates submicrometric iron oxide powders with granulated space-holder, yielding a dual-scale architecture of nanopores within the struts and micrometric pores replicating graphite morphology. Complete removal of the space holder was achieved at ≥800 °C with relatively fast heating rates (5 °C/min). Subsequent hydrogen treatment promoted complete reduction of hematite to metallic iron across the 850–1050 °C range, as confirmed by XRD and mass loss analyses. Based on thermogravimetric analysis data, kinetic parameters were determined and Avrami-Erofeev equation was found most suitable for describing each reduction step. Microstructural characterization revealed that densification of the struts is strongly dependent on sintering temperature and the phase-specific diffusion coefficients of iron. A non-monotonic mechanical response was observed across the temperature range, explained by the interplay between reduction kinetics, pore evolution, and phase-dependent diffusion. These findings demonstrate that porous iron structures can be tailored through space-holder engineering and submicrometric oxide powders combined with in-situ reduction–sintering. The methodology provides a scalable pathway for producing iron-based multiporous materials with controlled porosity and optimal mechanical strength.

## 1. Introduction

Porous materials are a class of engineered structures, where the porosity can be tailored to control mechanical, thermal, acoustic, and transport properties. This makes them attractive for a diversity of applications, such as thermal insulation, catalysis, filtration, biomedical scaffolds, and energy absorption systems [1–3]. Among them, metallic foams have received a particular interest from the research community due to their superior mechanical strength and toughness-to-weight ratio, in comparison to polymers and ceramics foams [4,5], as well as enhanced electrical and thermal conductivity [6–8].

Iron-based porous materials are particularly interesting as a material system due to the abundance, low cost and customizable mechanical properties by heat treatments or alloying. Applications include load-bearing lightweight components [3,4,9–11], filters [3], sound absorbers [8,9,12], electrodes in fuel cells [13], and support structures for catalysis [3,10,14]. Moreover, pure iron foams have been reported as promising for absorbable biomedical devices [3–5,15]. It is known that the properties of such porous and highly-porous materials are directly depending not only on the porosity content, but also on the porosity shape and size distribution, which can be tailored during the fabrication. Thereby, several fabrication methods have been investigated for porous ferrous structures, such as space-holder sintering [3,10,11], partial sintering [7,10], additive manufacturing [15], replication techniques [7,12] and injecting gas into molten metal and introducing chemical blowing agents during melting [8]. Foaming techniques are challenging to apply to iron because of its high density, elevated melting point, strong surface tension, and low melt viscosity. Powder metallurgy offers a more suitable route for producing porous metallic materials, enabling the fabrication of near-net-shape components with interconnected

* Corresponding author.
*E-mail address:* kaline.furlan@kit.edu (K.P. Furlan).

https://doi.org/10.1016/j.jmrt.2026.01.223
Received 29 September 2025; Received in revised form 27 January 2026; Accepted 28 January 2026
Available online 4 February 2026

porosity [8]. In addition, traditional powder-based methods are generally more cost-effective than 3D printing or laser sintering [5]. Among powder metallurgy techniques, space-holder sintering stands out for its simplicity, cost-effectiveness, and capability to control pore morphology and size distribution by selecting suitable space holders and processing parameters. Moreover, the type, shape, and volume fraction of the space holder influence not only the porosity content but also the pore connectivity and mechanical strength [11,16]. A significant challenge in the use of high-volume fractions of space holders lies in maintaining the continuity and mechanical strength of the metal struts between pores. In powder metallurgy, the particles that form the dense branches between pores (after space holder removal) must be smaller than the mean free path between space holder particles. Moreover, the smaller the particles, the greater the integrity of the network between the pores, as their sintering kinetics allows for fast densification [17]. Nevertheless, the use of fine powders presents several drawbacks, such as high cost and increased risk of oxidation and even pyrophoricity. As an alternative route, metallic iron foams with multiscale porosity could be obtained by in-situ sintering reduction of iron oxide submicrometric particles' porous bodies [4,11].

In this work, the fabrication of low-cost hazardous-free porous iron-based foams was investigated using hematite submicrometric particles ($Fe_2O_3$) as the raw material and graphite as a sacrificial space holder. We studied the in-situ reduction of $Fe_2O_3$ to metallic iron while simultaneously sintering the porous body to form a mechanically stable porous structure. Our results show that during the thermal treatment of in-situ reduction and sintering the graphite is removed to create micron-sized secondary porosity, while primary nano- and submicron porosity is formed due to the reduction process. The effect of the heat treatment process, namely temperature, dwell time and atmosphere, was analyzed with focus on the graphite oxidation and iron oxide reduction. The resulting iron foams were analyzed by scanning electron microscopy (SEM), X-ray diffraction (XRD), and density measurements to evaluate their structural and morphological features. Results show that the heat treatment temperature has a significant impact on the mechanical properties and porosity, however in a non-linear way, i.e. the best results are not obtained at the highest sintering temperature, but rather at 900 °C. This is associated with the enhanced sintering of the very fine, reduced iron particle network in the alpha phase.

## 2. Experimental procedure

Hematite powder (α-$Fe_2O_3$, LANXESS, Brazil) with an average particle size of 0.5 μm was used as the raw material for the matrix, while 42 vol% graphite powder (94140, Nacional de Grafite, Brazil) with an average particle size of 150 μm was employed as the space holder phase. Graphite, as a space holder, is advantageous due to its thermal stability and ease of removal by gasification under oxidizing atmospheres, as well as an aid agent in the reduction process. To avoid excessive shear during processing, the graphite flakes were mixed with 1.5 wt% of polyvinyl alcohol (PVA) at 80 °C prior to mixing. Graphite and PVA powders were loaded into a Y-mixer with steel balls at 1:5 ratio and mixed for a total of 45 min. The powder mix was then granulated using a 250 ml glass flask as the rotating drum. Paraffin wax (Exodo Cientifica, PH06788Ra) was used as granulation agent after its dissolution in hexane (Química Moderna, Analytic grade, QMA00001176101000) heated at 60 °C inside an ultrasonic bath, which was operated intermittently at 5 min interval until complete dissolution of the paraffin wax to avoid overheating of the organic solvent. Subsequently, the powder mixture (iron oxide + graphite) was added to the polymer solution at a solution to powder ratio of 25 ml:100 g with 3 wt% paraffin wax. After drying, granules were sieved between 250 and 500 μm.

Granulated powder samples were shaped by uniaxial pressing in a double action die at a pressure of 80 MPa. This relatively low compaction pressure was chosen to avoid excessive deformation of the space holder granules, whilst ensuring adequate green strength for subsequent handling. Samples of 9.9 mm diameter and 10 mm height were produced for all analyses except for the mechanical testing, for which 21 mm diameter and 7 mm height samples were manufactured [18]. After shaping, the samples were heat treated in a resistive tubular furnace (TU3513, Jung, Brazil). The heat treatment consisted of a com(4)bination of three processes: i) space holder removal in air; ii) in-situ reduction in hydrogen concomitantly with iii) sintering. In the first step, samples were heated at a rate of 5 °C/min up to 500 °C and held at this temperature for 60 min to remove PVA and paraffin. Samples were sintered in air at 750 °C, 800 °C, or 850 °C, using a dwell time of 2 h. This is followed by a further heating ramp in argon atmosphere to the target in-situ reduction and sintering temperature. Once the desired temperature was reached, the argon atmosphere was replaced with hydrogen gas. The investigated temperatures were 850 °C, 900 °C, 950 °C, and 1050 °C, with a dwell time of 1 h.

The density of heat-treated samples was assessed by geometrical method. The final porosity was measured by placing the samples in a sealed container under 130 Pa vacuum for 30 min. Distilled water was then introduced, and the specimens were kept under these conditions until complete saturation was achieved. The porosity was calculated from the mass difference between the dry and saturated samples. Microstructural characterization was performed by scanning electron microscopy (SEM) with coupled energy-dispersive X-ray spectroscopy (EDX) (VEGA3 LM-Tescan coupled with Oxford Instruments EDX). All samples were weighed before and after the reduction process, and X-ray diffraction (XRD) measurements (Rigaku Miniflex) were conducted to verify whether the reduction had been completed. Pore size, shape, and distribution were analyzed in metallographically prepared samples using LECO Image software. The image magnification was specifically selected so image quantification considered only the pores produced due to space holder removal. The mechanical properties were characterized by radial compression tests (Brazilian Test) using a universal testing machine at a cross speed of 0.8 mm/min up to failure. The reported values represent an average of six samples for each studied processing condition.

Thermogravimetric analysis (TGA) of the samples was carried out under a 100% hydrogen atmosphere using the $H_2$Secure system (Netzsch) integrated with the simultaneous differential thermal analysis device (STA 449 F3, Netzsch), ensuring safe operation under hydrogen conditions. Measurements were performed isothermally at 750 °C, 850 °C, 900 °C and 1050 °C. The samples were first heated under an argon atmosphere at a rate of 10 K $min^{-1}$ to the target temperatures and held for 30 min to stabilise. Subsequently, the gas atmosphere was switched to hydrogen for an additional 30 min (at 850 °C, 900 °C and 1050 °C) and 60 min (at 750 °C), as to precisely mimic the in-situ reduction sintering conditions.

The general form of the reaction kinetic equation can be expressed as (Eq. (1)):

$$\frac{d\alpha}{dt} = k(T)f(\alpha) \tag{1}$$

where $k$(T) is the temperature dependent reaction rate constant, $f(\alpha)$ is the reaction model, and α represents the degree of conversion.

The degree of conversion α, ranging from 0 to 1, was calculated from thermogravimetric measurements using NETZSCH Kinetics Neo software [19] (Eq. (2))

$$\alpha = \frac{m_0 - m_t}{m_0 - m_\infty} \tag{2}$$

where $m_0$, $m_t$ and $m_\infty$ are the mass at t = 0, at time t, and the end of the measurement, respectively.

For thermally controlled reactions, $k(T)$ is described by the Arrhenius equation (Eq. (3)):

$$k(T) = A.e^{-\frac{E_a}{RT}} \tag{3}$$

where $E_a$ represents the activation energy, $R$ is the universal gas constant, and $A$ is the pre-exponential factor, also known as the frequency factor.

## 3. Results and discussion

### 3.1. Powders

SEM analysis of the powders' morphology shows that they differ significantly in size (Fig. 1), with the iron oxide particles presenting a particle size distribution in the submicrometric scale range, while the graphite powder presents a size distribution in the micron scale range (nominal $d_{50}$ is 500 nm and 125 μm, respectively). It is known that the graphite particles, used as space holders, have low shear strength and thus, can suffer shear during the mixing step. The exemplary images in Fig. 1a and b shows that the excessive shear was effectively hindered by the PVA coating. The PVA coating is not soluble in organic solvents, which ensures that during the composite granulation in paraffin with hexane, the PVA coating is not dissolved. Fig. 1b shows SEM images after granulation, with a zoomed frame depicting the finer iron oxide particles adhered to graphite surfaces, demonstrating that the granulation process was effective for creating granular-like structures of graphite particles surrounded by iron oxide submicrometric particles. This microstructural design maximizes contact between the space holder and iron oxide submicrometric particles, which could be beneficial for the reduction process, later discussed. The granulation process also assures good flowability for the pressing step.

### 3.2. Space holder removal

Space holder removal was analyzed at different temperatures, namely 750 °C, 800 °C and 850 °C, in order to evaluate the effectiveness of removal, assessed by the mass loss in relation to the amount of graphite added in the mix (Fig. 2a). Samples sintered at 750 °C exhibited a ~75 % mass loss, with SEM analysis revealing the presence of residual graphite (Fig. 2c). For temperatures above 750 °C, graphite removal was complete, leaving secondary micron-sized pores behind, as exemplary shown for a sample treated at 850 °C in Fig. 2d. During space holder removal step in air, graphite reacts with atmospheric oxygen, producing CO and $CO_2$ as byproducts. As displayed in Fig. 2b, the ratio of CO to $CO_2$ depends on temperature, governed by the Boudouard equilibrium: at higher temperatures, CO production is favored, while $CO_2$ predominates at lower temperatures. Mass loss is more pronounced at higher temperatures since CO formation requires less oxygen per carbon atom than $CO_2$. As CO formation reaction is endothermic, its rate increases with the temperature.

We hereby demonstrate that the oxidation of graphite as a space holder is an approach that allows for high heating rates (5 °C/min) to be used during space holder removal, even using a space holder amount as high as 42 vol% This rate is significantly higher than the typical values reported in the literature, which generally range from 1 to 3 °C/min for space holder removal processes [20,21] or requiring dwell times as long as 21 h [22]. Furthermore, unlike other space-holder removal methods, such as the dissolution of salts or polymers, graphite oxidation enables the formation of a gas directly from the solid particles, eliminating the need of chemical leaching and concerns related to liquid-phase interactions, such as capillary effects, swelling, and bubbles.

Additionally, the presence of nanopores (primary pores) was also observed (Fig. 2e), being associated with the interparticle spacing between the iron oxide submicrometric particles. As in this temperature only partial sintering is expected for iron oxide [23], this porosity is not eliminated. For further investigations regarding the reduction of the iron oxide partially-sintered porous body with hydrogen, a temperature of 850 °C was selected, as it ensured complete removal of the graphite space holder.

### 3.3. Reduction in hydrogen

The investigation regarding the iron oxide reduction process using hydrogen was carried out at temperatures of 850 °C, 900 °C, 950 °C, and 1050 °C. It is essential to point out that for all these temperatures, the samples were heated in a neutral gas flow (argon) until reaching the intended isothermal plateau temperature for the reduction. At this point, the gas was switched to hydrogen, and the temperature was maintained for 1 h. This procedure was designed to ensure that the mass loss analyzed during this stage would be related to the reduction. All samples analyzed obtained a mass loss corresponding to 100 % reduction,

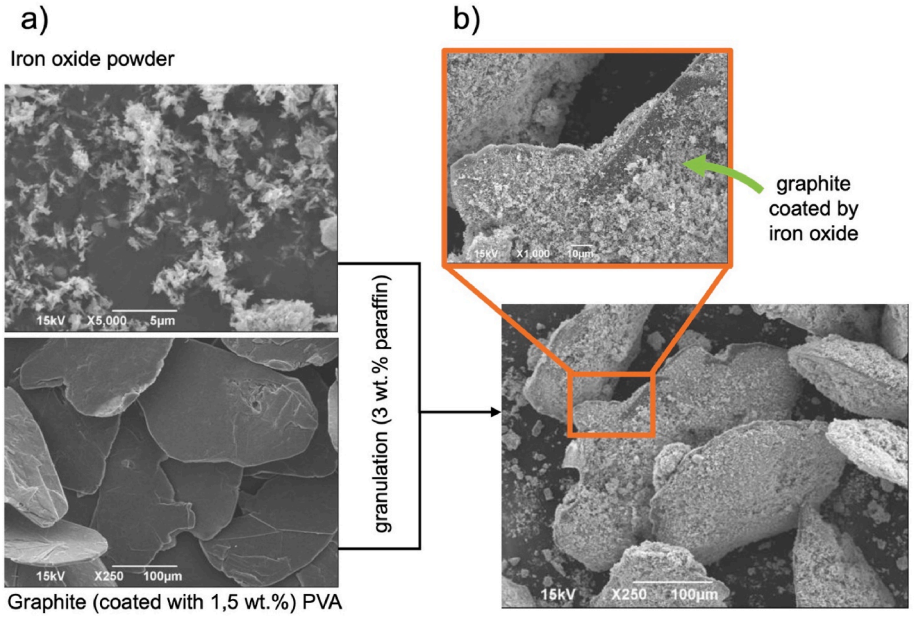


**Fig. 1.** a) SEM micrographs of the raw materials: iron oxide powder (top) and graphite coated with 1.5 wt% PVA (bottom), highlighting the significant size difference between particles (iron oxide: nanometer scale, graphite: micrometer scale). b) SEM image of granulated composite powder after the addition of 3 wt% paraffin, showing fine iron oxide particles adhered to the graphite surfaces, improving flowability and ensuring uniform distribution during compaction.

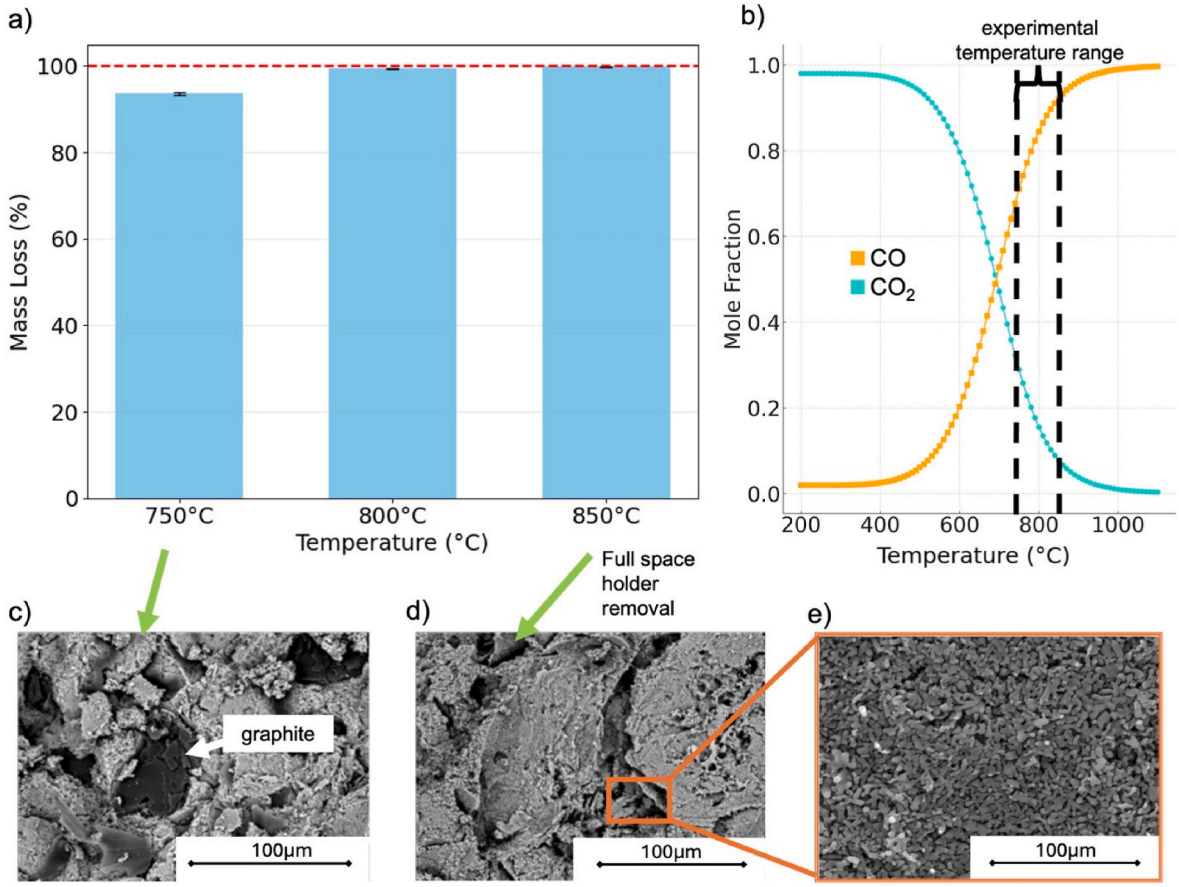


**Fig. 2.** Mass loss during space holder removal and sintering behavior. (a) Mass loss (%) as a function of temperature (750–850 °C), showing residual graphite at 750 °C and complete removal above this temperature. (b) Boudouard equilibrium diagram showing the temperature-dependent ratio of CO and $CO_2$ formation during graphite oxidation, with CO formation increasing at higher temperatures (calculated using Themo-Calc TCFE14 database). (c) SEM image at of residual graphite in the sample heat treated at 750 °C. (d) SEM image for samples heat treated at 850 °C showing secondary pores formed after complete graphite removal. (e) High-magnification SEM image illustrating smaller pores resulting from partial sintering of oxide particles.

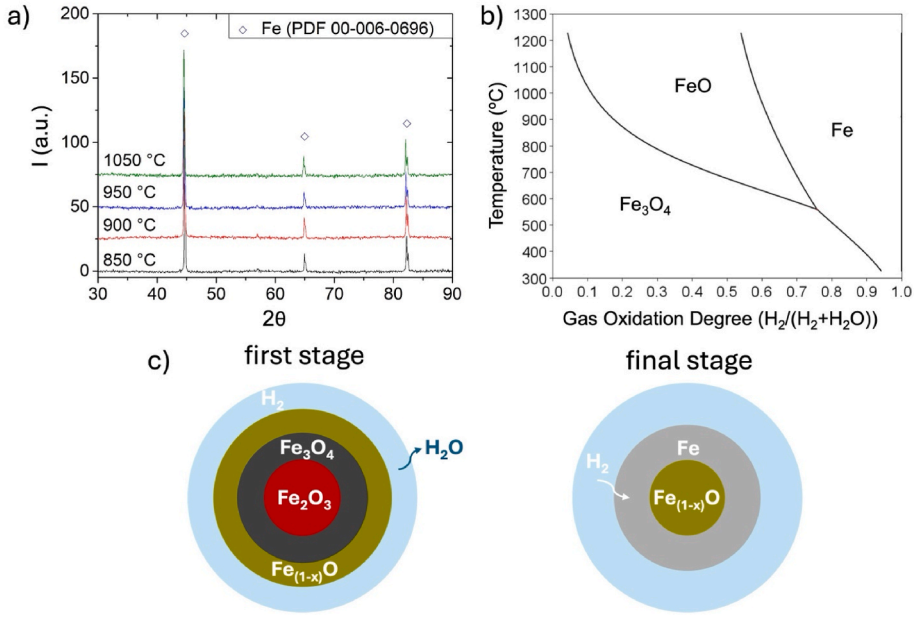


**Fig. 3.** (a) X-ray diffraction (XRD) patterns of iron oxide samples subjected to reduction at different temperatures (850 °C-1050 °C) reveal that all iron oxide porous structures were converted into metallic Fe, with reference peaks for Fe (PDF# 00-006-0696) indicated. (b) Baur–Glässner diagram showing the thermodynamic stability regions of FeO, $Fe_3O_4$, and Fe under $H_2$–$H_2O$ (calculated using Themo-Calc TCFE14 database) Schematic of the two-stage reduction mechanism: in the first stage, $Fe_2O_3$ is reduced to $Fe_3O_4$ and FeO, and in the second stage, $Fe_{(1-x)}O$ is reduced to metallic Fe.

calculated based on the amount of iron oxide added to the initial mix. Furthermore, XRD measurements (Fig. 3a) have confirmed that the peaks observed in all samples correspond to iron (indexed pattern PDF 00-006-0696), attesting for the successful fabrication of an iron skeleton via reduction of the initial iron oxide porous body.

Based on these results and in the literature [24–26], we suggest the following path for the reduction process from $Fe_2O_3$ to Fe in hydrogen for the practiced temperature range:

1. Hematite to Magnetite:

$$3\ Fe_2O_3 + H_2 \rightarrow 2\ Fe_3O_4 + H_2O$$

2. Magnetite to Wüstite

$$(1\text{-}x)Fe_3O_4 + (1\text{-}4x)H_2 \rightarrow 3Fe_{(1\text{-}x)}O + (1\text{-}4x)H_2O$$

3. Wüstite to Metallic Iron:

$$Fe_{(1\text{-}x)}O + H_2 \rightarrow (1\text{-}x)Fe + H_2O$$

This suggested reaction process is schematically illustrated in Fig. 3c, while Fig. 3b presents the Baur–Glässner diagram for iron oxides as a function of the percentage of $H_2$ in the $H_2O + H_2$ atmosphere. It can be observed that at temperatures above approximately 600 °C, $Fe_3O_4$ is progressively reduced to $Fe_3O_4$ and then to $Fe_{(1\text{-}x)}O$ before forming metallic iron. Below this temperature, $Fe_3O_4$ transitions directly to metallic iron without passing through the $Fe_{(1\text{-}x)}O$ intermediate phase [27].

Moreover, an early study by Hammam et al. [26] for hydrogen reduction of $Fe_2O_3$ micrometric powder compacts in the temperature range of 800–1100 °C showed that for any fixed temperature, the reduction rate is initially high but decreases over time, indicating a two-stage reduction process. The early and intermediate reduction phases involve transformation from $Fe_2O_3$ to $Fe_3O_4$ and then to $Fe_{(1\text{-}x)}O$, whereas the final stage involves the slower transformation of $Fe_{(1\text{-}x)}O$ to metallic Fe [27]. Furthermore, the calculated activation energies by Hammam et al. [26] confirm that hydrogen is a more efficient reducing gas than carbon monoxide, i.e. 39.23 and 54.19 kJ/mol. Arrhenius analysis shows distinct activation energy (Ea) values for the initial (5–15 %) and final (85–95 %) reduction stages, confirming the shift in controlling mechanisms, i.e. 28.34 and 41.15 kJ/mol, respectively [26]. The activation energies (Ea) help clarify the reaction mechanisms involved in the reduction of the oxide particles by hydrogen. As illustrated in Fig. 3c, the early stages of reduction are governed by mixed control, in which the reaction rate depends both on the diffusion of hydrogen through the surrounding atmosphere and on its chemical reaction at the oxide particle surface. Then, $Fe_{(1\text{-}x)}O$ starts being reduced to iron and a dense layer of metallic iron (Fe) forms around an unreacted $Fe_{(1\text{-}x)}O$ core. At this point it was observed by the authors that, the controlling step becomes the interfacial chemical reaction at the boundary between $Fe_{(1\text{-}x)}O$ and Fe, where the reaction occurs more slowly due to limited reactive surface and the slow diffusion of hydrogen through the iron layer in comparison to the porous iron oxide layer. Therefore, finer particles — especially submicrometric ones — will have a very thin 'Fe barrier' blocking diffusion, thus reducing the rate associated with the slowest step [25].

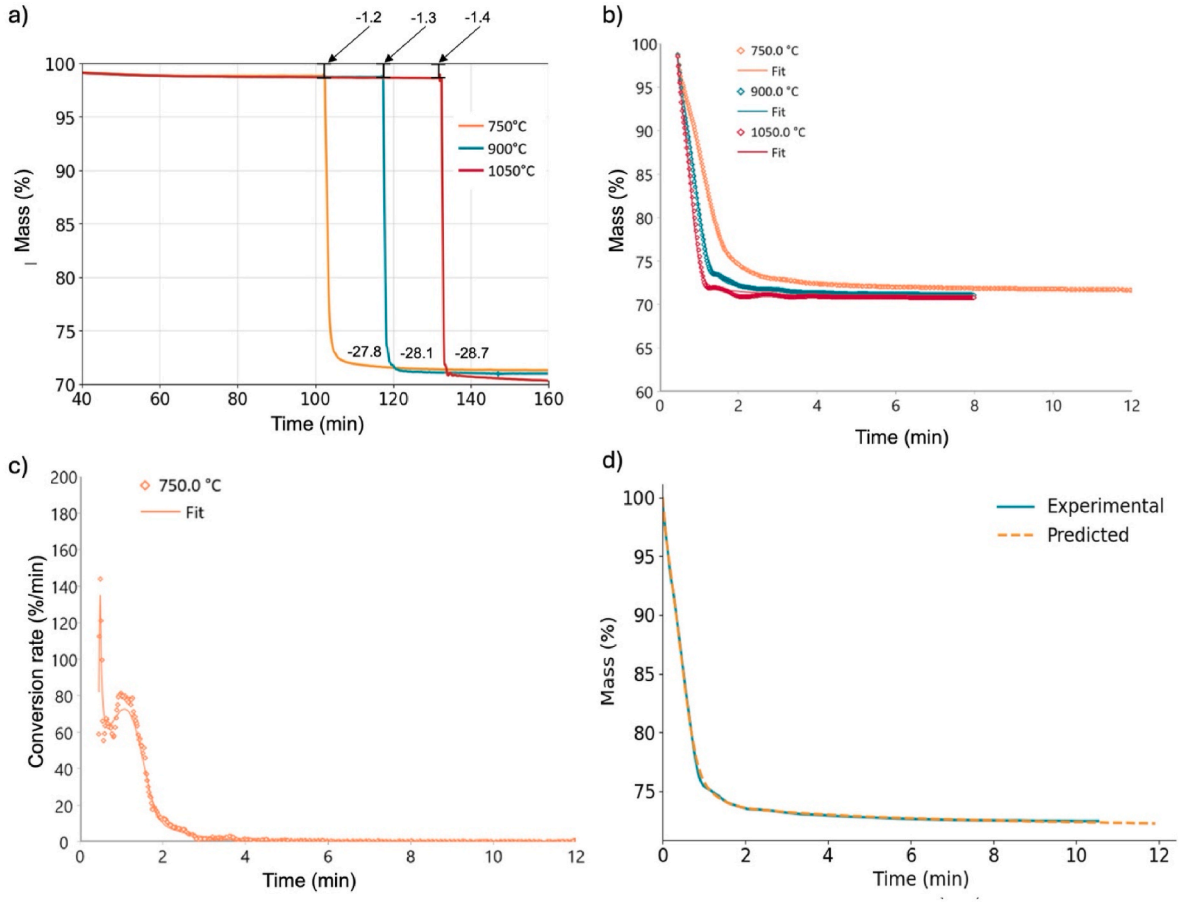


**Fig. 4.** (a) Thermogravimetric results of the reduction of the samples under a 100% hydrogen atmosphere at 750 °C, 900 °C and 1050 °C% (b) Kinetic evaluation of experimental thermogravimetric data by the reduction of $Fe_2O_3$ samples under a 100% hydrogen atmosphere at 750 °C, 900 °C and 1050 °C: rhombus – experimental data; solid lines: calculated curves; (b) Conversion rate of $Fe_2O_3$ powder measured at 750 °C; (d) Experimental and predicted TGA mass change (signal) during $Fe_2O_3$ reduction under 100% $H_2$ at 850 °C.

The thermogravimetric analysis of the $Fe_2O_3$ powder (Fig. 4) performed in this work reveals two distinct mass-loss events during the imposed thermal cycles. Upon heating under an argon atmosphere, a mass loss of 1.2% at 750 °C, 1.3 % at 900 °C and 1.4% at 1050 °C was observed, likely due to the thermal decomposition of iron carbonates, hydroxides, and other impurities, such as adsorbed water. Therefore, the initial mass of $Fe_2O_3$ should be corrected accordingly to enable precise determination of the mass change (%) during hydrogen reduction. Two runs were performed for each temperature, and in both cases the curves show good reproducibility of the obtained results. Importantly, during the 30-min isothermal hold under argon at the maximum temperature, no additional mass loss was observed, indicating that reduction does not initiate in the absence of hydrogen. Once the atmosphere is switched from Ar to $H_2$, the system undergoes an abrupt mass loss corresponding to 27.8% (at 750 °C), 28.1 % (at 900 °C), 28.7 % (at 1050 °C) (Fig. 4a). These values of mass loss were corrected according to the mass of purified $Fe_2O_3$. All these results are lower than the theoretical value of the reduction reaction of $Fe_2O_3$ to Fe 30.06%, which indicates on the presence of additional impurities in the sample and explains the differences between different temperature steps.

Fig. 4b shows the experimental TGA isotherms of the reduction of $Fe_2O_3$ samples under 100% hydrogen atmosphere at 750 °C, 900 °C, and 1050 °C, used for kinetic evaluation. In accordance with the recommendations of the International Confederation for Thermal Analysis and Calorimetry (ICTAC), three isothermal programs were performed [28]. It should be noted that the TG curves at 900 °C and 1050 °C exhibit small signal fluctuations. Similar fluctuations were also observed in the baseline obtained from empty-crucible corrections; therefore, these effects were attributed to instrumental noise and were not considered in the modelling. The reduction of $Fe_2O_3$ powder occurs in two main steps, as illustrated in Fig. 4c, where the conversion rate is defined as the first derivative of conversion with respect to time. The initial step comprises previously mentioned chemical reactions 1 and 2. Under a 100 % $H_2$ atmosphere, the kinetics are too fast to resolve these two steps individually. The second reduction step corresponds to chemical reaction 3; however, this step separates into two sub-stages because the reduction rate decreases significantly during its final portion. Similar behaviour was considered in Refs. [29,30]. In multi-step reactions (model-fitting), the number of kinetic triplets equals the number of steps. This approach was recommended by the Kinetics Committee of the ICTAC (International Confederation for Thermal Analysis and Calorimetry) [31]. This multi-step process can be described using a three-step kinetics model. The reaction rate of each step, j, is described by the function (Eq (4)) [32]:

$$\text{Reaction Rate}_j = A_j \cdot f\left(e_j, p_j\right) \cdot e^{\left(-\frac{E_j}{RT}\right)} \tag{4}$$

$A_j$: pre-exponential factor.

$E_j$: energy activation [J/mol].

T: temperature [K].

R: gas constant (8.314 J/K.mol).

f ($e_j$,$p_j$): function dependent on the concentration of the initial reactant $e_j$ and the concentration of product $p_j$

**Table 1**
Kinetic parameters obtained from model-based analysis of $Fe_2O_3$ reduction under 100%-$H_2$.

| Reaction step | A→B | B→C | C→D |
|---|---|---|---|
| | Cn | An | Fn |
| Activation energy [kJ/mol] | 29.90 | 29.49 | 48.36 |
| Log (Pre- Exp) Log (1/s) | 0.785 | −0.770 | 0.666 |
| Dimension | | 7.318 | |
| Reaction order | 2.806 | | 0.676 |
| Log (Autocat Pre- Exp) | 0.630 | | |
| Coefficient of determination ($R^2$) | 0.999 | | |

Table 1 summarizes the kinetic parameters obtained from model-based analysis of $Fe_2O_3$ reduction under 100% $H_2$. The table summarizes activation energies, pre-exponential factors, reaction orders and correlation coefficients ($R^2$) for each reaction step. Reaction types include: An – n-dimensional nucleation (Avrami–Erofeev), Cn – n-th-order reaction with autocatalysis by product, and Fn – n-th-order reaction. These models were evaluated among several candidates, with Avrami-Erofeev nucleation providing the best fit for the studied reduction steps. The results show good agreement between the measured and calculated data, with a coefficient of determination $R^2 = 0.999$.

The kinetic parameters for the reduction of iron oxides can vary and are influenced by multiple factors, including operational parameters (such as temperature, pressure, and gas composition), material properties (such as grain size, morphology, and porosity), and the kinetics analysis approach (either model-free or model-based (multi-step model fitting)) [27,29,31]. Fig. 4d shows the additional experimental TGA values for the reduction of $Fe_2O_3$ in 100% $H_2$ at 850 °C, which were obtained to validate the kinetic parameters. The mass change is shown in orange (experimental data) and green (predicted). The validation results indicate good agreement between experimental and predicted data, both qualitatively and quantitatively. The activation energies obtained from the model-based analysis (Table 1) fall within the same characteristic ranges reported in the literature for $Fe_2O_3$ reduction in pure $H_2$. The first two steps (A→B, B→C) show activation energies, which correspond well to the initial and intermediate reduction stages reported in the literature 28.34 kJ/mol [26] and 25.3 and 25.7 kJ/mol [29,30]. In the work of Wang et al. [29], the measurements were performed under 10 % $H_2$, and two sub-stages of reaction 3 were distinguished. However, the authors did not report the activation energy of the final slow stage. In contrast, our analysis resolves this last step and yields an activation energy of 48.36 kJ/mol, which agrees reasonably well with the value of 41.15 kJ/mol reported for the corresponding late-stage reduction step in Ref. [25].

A recent study by Murakami et al. [11] demonstrated that highly porous iron can also be produced through the direct carbothermic reduction of hematite using different carbon sources: graphite, coal, and biomass char. A key aspect of this approach is that the proportion between the oxide and the carbonaceous material must be fixed to ensure complete reduction and full removal of the carbon source. As a result, the total amount of porosity attainable is inherently linked to the reduction/sintering pathway and to the swelling or shrinkage behavior of the compact, instead of the amount of added space holder.

Murakami et al. [11] showed that both the carbon source and the reduction mechanism strongly influence whether the compact expands or contracts during reduction. When using submicrometric $Fe_2O_3$ powders combined with biomass char, they achieved extreme swelling and porosities up to ~98%, which was the main objective of the study. In contrast, when coal or graphite were used as space holders, no ultra-high porosity was observed, and the samples retained their original geometry.

Among all carbon sources investigated, graphite exhibited the highest removal rate, largely because it contains fewer impurities (such as volatile matter, oxides, and sulfur) compared to coal and biomass char. However, because the mass ratio between graphite and hematite must remain fixed to guarantee complete removal, porosity cannot be freely adjusted by simply varying the graphite content; instead, different porosity levels must be achieved indirectly through the swelling behavior of the system using biomass char.

### 3.4. Sintering

The morphology of the porous structures after the reduction process can be visualized in Fig. 5. The sintering process of particles takes place concomitantly to the reduction process and a clear microstructural difference can be seen from Fig. 5a–e (lowest temperature) up to Fig. 5d–h (highest temperature). The sintering process is mostly relevant for the

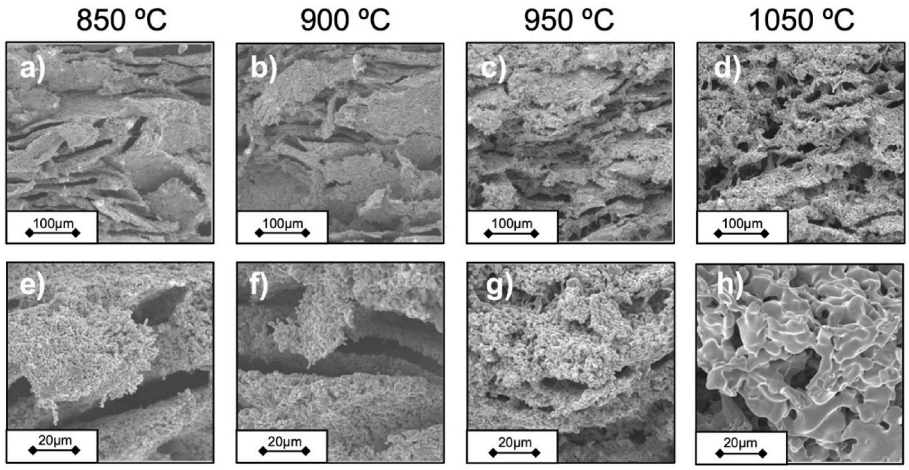


**Fig. 5.** SEM micrographs showing the microstructural evolution of samples sintered at 850 °C, 900 °C, 950 °C, and 1050 °C a), b), c), d) at 100 µm scale, respectively and e), f), g), and h) at 10 µm scale, respectively. The progression from 850 °C (a, e) to 900 °C (b, f) illustrates increased densification and reduced primary porosity with temperature. From 950 °C (c, g), primary porosity increases and at 1050 °C there seem to be new secondary pores (d) and increased coalescence of powder particles (h).

already-reduced particles, i.e. iron submicrometric particles which are known to have a higher sinterability than iron submicrometric nanoparticles [23,33]. As they are reduced to iron, particle contacts (necks) form and grow, resulting in a denser microstructure for the primary porosity (nanoscale) observed within the struts, similar to what has been reported by Daneshmandian et al. [4]. The final sample structure — and resulting mechanical strength, later discussed — derives from the combined effect of the primary pores, which depend on strut densification, and the secondary pores, formed by the space holder. Ideally, we aim to maximize densification within the struts while preserving the functional porosity introduced by the space holder. This rationale guided the selection of submicrometric powders, as their small size allows them to have high packing densities in the interstitial regions between space-holder particles and ensures high sinterability, promoting strut consolidation without compromising the designed macro-porosity. In the following paragraphs, we discuss the microstructural evolution from the point of view of the porosity – nanoscale primary porosity and microscale secondary porosity – in detail.

For the samples processed at 850 °C, it is possible to observe in the magnified strut region of Fig. 5e that the iron oxide particles still retain the appearance of discrete entities in the 100 nm order of magnitude, meaning that sintering remains limited at this temperature and thus, primary porosity is still majorly present. As the temperature increases to 900 °C, the porous structure displayed in Fig. 5f shows signs of enhanced densification, and the pore network becomes more compact and interconnected within the struts. At 950 °C (Fig. 5g), the densification within the struts is lower than in samples sintered at 900 °C. At 1050 °C the struts display particle coarsening and a clear elimination of the primary pores.

This nonlinear densification behavior between 900 °C and 950 °C can be associated with the influence of the diffusion coefficient in the mass transport mechanisms. As known, the self-diffusion coefficient of iron varies with the iron phase crystal structure. At 900 °C, sintering is more effective because self-diffusion in the α-phase ($1{,}89 \times 10^{-15}$ [34]) is higher than in the γ-phase at 950 °C ($3{,}54 \times 10^{-17}$ [34]). With a larger temperature increase to 1050 °C the increase in mass transport due to temperature surmounts the effect of the phase transition, thus leading to a higher density within the primary particles network.

Concomitantly, the secondary porosity formed by the space holder also evolves, however at a different scale following the initial space holder size in the order of hundreds of micrometers. To illustrate this secondary porosity structure, Fig. 6 shows exemplary the detailed analysis of the sample reduced at 900 °C in hydrogen after the space holder removal step. The cross section SEM micrograph in Fig. 6a displays the elongated nature of the pores, as seen by their irregular, elongated shapes distributed throughout the matrix, which is a clear reproduction of the shape of the space holder particles as previously observed in Figs. 1a and 2d. The histogram and cumulative frequency distribution (Fig. 6b) reveal that the distribution of pore lengths (represented in blue) is skewed towards larger sizes, with the majority of pores falling in the range of 150–250 µm. Conversely, the pore width (green) is predominantly concentrated below 100 µm, attesting for the

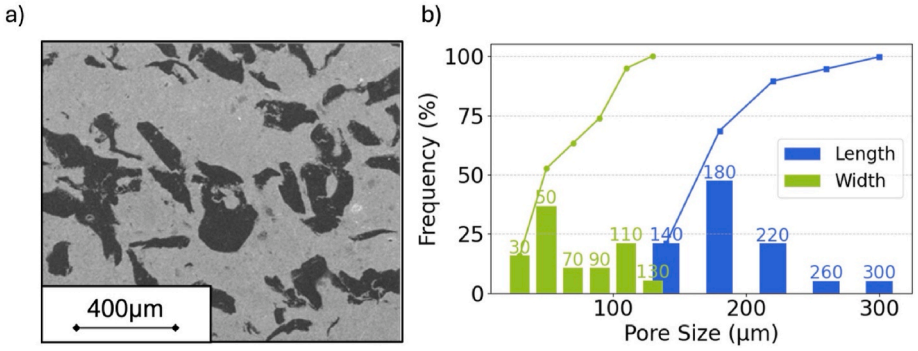


**Fig. 6.** (a) The SEM of the microstructure with visible pores corresponding to the analyzed pore sizes and its respective shape and elongation factors. The dark regions correspond to the pores, while the lighter regions represent the solid material. (b) Pore width and length distribution for samples oxidized at 850 °C and sintered at 900 °C. The green bars represent pore size length (µm) while the blue bars represent pore size width (µm).

elongated pore morphology. These results are confirmed by the shape factor and elongation factor, corresponding to 0.47 and 0.38, respectively.

### 3.5. Mechanical properties

As mentioned before, the resulting mechanical strength (Fig. 7a) derives from the combined effect of the primary pores, which depend on strut densification, and the secondary pores, formed by the space holder. Ideally, we aim to maximize densification within the struts while preserving the functional porosity introduced by the space holder with the goal of achieving an optimum relation between total porosity and mechanical properties. The porosity values shown in Fig. 7a represent the total porosity across the entire sample, meaning it reflects a combination of both macro- and nanopores. Our results demonstrate that for samples processed at 850 °C, the fracture strength is moderate (~0.6 MPa), mainly due to limited sintering between powder particles: the segment size is the smallest, indicating insufficient connection among the particles, and porosity is the highest (42.04 %). At 900 °C, fracture strength reaches a peak (~1.1 MPa), due to the increase in the struts' densification, where the samples display the lowest overall porosity of 36.95%. Moreover, as demonstrated in Fig. 7b the micropores evolve to a less elongated shape (increase in shape factor) in comparison to the lowest temperature sample, potentially contributing to the gain in strength. At 950 °C, fracture strength drops (~0.4 MPa), which is associated to an overall increase of the porosity to 41.10 %. As previously discussed, this increase in porosity is a combination of the decrease in mass transport due to reduced diffusion, greatly influencing sintering and densification. The reduction in mass transport also leads to a less rounded morphology of the secondary pores, as evidenced by the decrease in shape factor shown in Fig. 7b. This effect may have contributed to the decrease in mechanical strength, since more elongated pores can act as stress concentrators. At 1050 °C, fracture strength is partially recovered (~1.0 MPa), which is associated with the presence of a clearly densified skeleton formed by the sintering of the reduced iron particles (see Fig. 5h) and rounding of pores (highest shape factor), which compensates for the fact that overall porosity associated particularly to secondary pores is still high (41.96%).

A recent study by Daneshmandian et al. [4] demonstrated that iron foams can be also be fabricated using a NaCl space-holder route followed by sintering and hydrogen reduction of $Fe_2O_3$ powders. Their process yielded foams with ~60% porosity, combining large macropores defined by the salt template with smaller residual pores inside the struts, resulting in a hierarchical architecture similar to that obtained in the present study. The choice of a salt-based space holder implies in intermediate thermal and dissolution stages. After cold compaction, the samples were pre-baked at 800 °C for 2 h, followed by a salt-removal step using immersion in distilled water at 80 °C for 3 h under constant magnetic stirring. When mass-loss measurements confirmed that >90% of the salt had been dissolved were the samples allowed to proceed to the next steps. The compacts were then sintered at 950 °C for 2 h to consolidate the $Fe_2O_3$ particles. Reduction to metallic iron was carried out in a hydrogen atmosphere at 600 °C for 1 h, followed by an additional 4 h of heat treatment at 950 °C in hydrogen to complete the transformation and strengthen the struts. The analysis of mass changes before and after the reduction stage point to a reduction degree of 90%. Their compressive strength testing showed that the foams produced display a yield point around ~15–20 MPa.

A study by Carpenter et al. [35] produced hierarchical porous iron structures using particle-stabilized foams combined with direct ink writing (DIW), reduction, and sintering. Their ink is formulated from magnetite ($Fe_3O_4$) microrods with hexylamine surface modification and water. Mechanical frothing incorporates stable air bubbles into this suspension, generating a foam that can be extruded through sub-millimeter nozzles. After printing, the dried oxide structures are reduced for 30–40 h under 5 % $H_2$/95% $N_2$ gas, and sintered at temperatures between 690 °C and 1000 °C. The printed parts develop three hierarchical porosity levels: millimeter-scale pores defined by the DIW toolpath, bubble-templated macropores (~45–125 μm depending on particle concentration), and microporosity formed during reduction of $Fe_3O_4$ to metallic iron. The final metallic phase foams display porosity between ~92 % and 95 %. Chemical analysis also revealed that the resulting metal contains ~0.20 wt% C, classifying it as a low-carbon steel. The optimized two-step treatment (690 °C reduction for 40 h + 850 °C sintering) produced samples with a yield strength of around 1.25 MPa.

Direct comparison with those results is not possible, since our mechanical tests were performed under radial compression, which introduces an additional tensile component in the struts of the porous structure. Furthermore, the relationship between porosity, pore size, and mechanical strength is highly application-specific. Therefore, when contrasted with the rest of the literature, what stands out most in our case is the degree of tailoring enabled by this processing route, particularly through the controlled adjustment of graphite content and sintering conditions. Combined with the significantly higher removal rates during the space holder removal step, which can be especially beneficial for the large-scale production of porous components.

## 4. Conclusion

This study demonstrates a cost-effective methodology for producing hierarchically porous iron-based structures through the integration of in-situ reduction and sintering of hematite powders with a sacrificial graphite space holder.

The strategy successfully combined submicrometric oxide precursors and granulated space-holder design, enabling the formation of a dual-scale (hierarchical) porous architecture, with primary nanopores within the struts and secondary micrometric pores replicating the graphite granules morphology. This hierarchical porosity enables enhanced diffusion, mass transport and tailored mechanical behavior

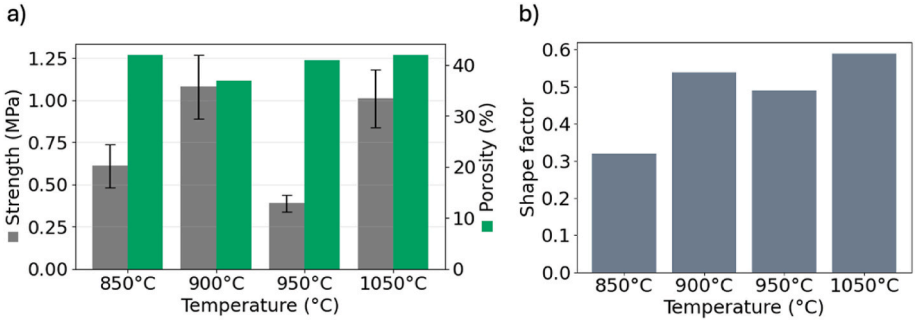


**Fig. 7.** (a) Compressive strength (gray bars, left axis) and porosity (green bars, right axis) of sintered samples as a function of sintering temperature (b) *Shape-factor values of the secondary pores as a function of reduction temperature.*

[3]. Complete graphite removal was achieved via oxidation at moderate temperatures and relatively fast heating rates (5 °C/min). Compared with traditional leaching or polymer burnout, graphite oxidation provides a faster and cleaner route for macropore formation [3]. It is also significantly faster than the ice templating and lyophilization steps used in freeze-casting [3]. Complete reduction of hematite to metallic iron was confirmed across the 750–1050 °C range. The reduction kinetics of $Fe_2O_3$ in 100 % $H_2$ were captured by the applied multistep kinetic model, yielding activation energies of 29.90 kJ/mol and 29.49 kJ/mol for the first two consecutive steps and 48.36 kJ/mol for the final slow stage of the reduction reaction. The model was additionally validated using an independent measurement at 850 °C, which showed very good agreement with the predicted reduction behavior based on the derived kinetic parameters.

Microstructural and mechanical analyses revealed that the densification behavior of the struts strongly depends on the sintering temperature and phase-dependent diffusion of iron. At 900 °C, sintering was most effective due to the higher self-diffusion coefficient of α-Fe compared to γ-Fe, resulting in optimal microstructural consolidation, reduced porosity (~37%), and the highest compressive strength (~1.1 MPa). At 1050 °C, the increase in mass transport with temperature overcame the effect of the phase transition, leading to renewed densification. This non-monotonic trend in mechanical performance is explained by the interplay of reduction kinetics, pore formation mechanisms, and phase-specific diffusion, validating the proposed approach as a scalable route to tailor porous iron materials for applications such as acoustic damping, filtration, and thermal insulation.

## Declaration of competing interest

The authors declare the following financial interests/personal relationships which may be considered as potential competing interests: The authors Klein and Mocellin declare to have applied for a patent regarding the application of such iron-based multiporous structures as acoustic insulators (US9969003B2).

## Acknowledgements

The authors acknowledge CNPq (National Council for Scientific and Technological Development) for financial support. Furlan gratefully acknowledges the financial support from Deutsche Forschungsgemeinschaft (DFG, German Research Foundation) through the Cluster of Excellence EXC3120 BlueMat: Water-Driven Materials. We would like to further express our gratitude to Dr. Jan Hanss (NETZSCH A&T, Germany) and Dr. Elena Moukhina (NETZSCH A&T, Germany) for their invaluable support and insightful discussions related to the thermogravimetric measurements and kinetic calculations.

## References

[1] Gibson LJ, Ashby MF. Cellular solids. Cambridge University Press; 1997. https://doi.org/10.1017/CBO9781139878326.
[2] Banhart J. Manufacture, characterisation and application of cellular metals and metal foams. Prog Mater Sci 2001;46:559–632. https://doi.org/10.1016/S0079-6425(00)00002-5.
[3] Yang Y, Li L-H, Li Y, Rooke JC, Sanchez C, Su B-L, Yang X-Y, Chen L-H, Ment Sanchez C. Hierarchically porous materials: synthesis strategies and structure design. Chem Soc Rev 2017;46:481. https://doi.org/10.1039/C6CS00829Aï.
[4] Z. Daneshmandian, M.H. Paydar, New method for fabrication iron metal foam through powder metallurgy route, (n.d.). https://doi.org/10.22055/jomi.2025.48793.1026.
[5] Salama M, Vaz MF, Colaço R, Santos C, Carmezim M. Biodegradable iron and porous iron: mechanical properties, degradation behaviour, manufacturing routes and biomedical applications. J Funct Biomater 2022;13. https://doi.org/10.3390/jfb13020072.
[6] Duarte I, Banhart J. A study of aluminium foam formation—kinetics and microstructure. Acta Mater 2000;48:2349–62. https://doi.org/10.1016/S1359-6454(00)00020-3.
[7] Lefebvre L-P, Banhart J, Dunand DC. Porous metals and metallic foams: current status and recent developments. Adv Eng Mater 2008;10:775–87. https://doi.org/10.1002/adem.200800241.
[8] Hassan A, Alnaser IA. A review of different manufacturing methods of metallic foams. ACS Omega 2024;9:6280–95. https://doi.org/10.1021/acsomega.3c08613.
[9] Smith BH, Szyniszewski S, Hajjar JF, Schafer BW, Arwade SR. Steel foam for structures: a review of applications, manufacturing and material properties. J Constr Steel Res 2012;71:1–10. https://doi.org/10.1016/j.jcsr.2011.10.028.
[10] Li-Yin G, Hao-Kun Y, Xuan C, Wei-Dong T, Xing-Ming H, Zhi-Quan L. The development of porous metallic materials: a short review of fabrication, characteristics, and applications. Phys Scr 2023;98:122001. https://doi.org/10.1088/1402-4896/ad086c.
[11] Murakami T, Takahashi T, Fuji S, Maruoka D, Kasai E. Development of manufacturing principle of porous iron by carbothermic reduction of composite of hematite and biomass char. Mater Trans 2017;58:1742–8. https://doi.org/10.2320/matertrans.M2017232.
[12] Quadbeck P, Stephani G, Kümmel K, Adler J, Standke G. Synthesis and properties of open-celled metal foams. Mater Sci Forum 2007;534–536:1005–8. https://doi.org/10.4028/www.scientific.net/MSF.534-536.1005.
[13] Wu Z, Ni Z, Qin M, Zhang B, Liu Q, Zhao F, Liu G, Long P, Li F, Yu H, Song H, Feng Y, Feng W. High-power microbial-fuel-based hybrid cells with three-dimensional graphene-coated iron foam as an anode control Fe 3 + release. SmartMat 2024;5. https://doi.org/10.1002/smm2.1267.
[14] Li D, Cao Y, Ye R, Wang Y, Liu X, Zhou L, Wu D, Sun X, Zhao Z. Self-supported transition-metal-based electrocatalysts on iron foam for water splitting. Chem Eng J 2025;516:163602. https://doi.org/10.1016/j.cej.2025.163602.
[15] Salama M, Vaz MF, Colaço R, Santos C, Carmezim M. Biodegradable iron and porous iron: mechanical properties, degradation behaviour, manufacturing routes and biomedical applications. J Funct Biomater 2022;13:72. https://doi.org/10.3390/jfb13020072.
[16] Mahto RP, Bhadauria A, Bandhu D, Karmkar S. A study on porosity and mechanical properties of the open aluminum metal foam through spark plasma sintering SDP technique. Int J Adv Manuf Technol 2025;136:4407–17. https://doi.org/10.1007/s00170-025-15077-x.
[17] Wu Y, Guo K, Ni J. Characterization of particle size effects on sintering shrinkage and porosity in stainless steel metal injection molding using multi-physics simulation. Materials 2024;17:5691. https://doi.org/10.3390/ma17235691.
[18] Shetty DK, Rosenfield AR, Duckworth WH. Mixed-mode fracture of ceramics in diametral compression. J Am Ceram Soc 1986;69:437–43. https://doi.org/10.1111/j.1151-2916.1986.tb07441.x.
[19] NETZSCH-Gerätebau GmbH. Kinetics neo. https://kinetics.netzsch.com/. [Accessed 4 January 2026].
[20] Supriadi S, Suharno B, Hidayatullah R, Maulana G, Baek ER. Thermal debinding process of SS 17-4 PH in metal injection molding process with variation of heating rates, temperatures, and holding times. Solid State Phenom 2017;266:238–44. https://doi.org/10.4028/www.scientific.net/SSP.266.238.
[21] Chen Y, Kent D, Bermingham M, Dehghan-Manshadi A, Dargusch M. Manufacturing of biocompatible porous titanium scaffolds using a novel spherical sugar pellet space holder. Mater Lett 2017;195:92–5. https://doi.org/10.1016/j.matlet.2017.02.092.
[22] Arifvianto B, Zhou J. Fabrication of metallic biomedical scaffolds with the space holder method: a review. Materials 2014;7:3588–622. https://doi.org/10.3390/ma7053588.
[23] Yamaguchi T, Kosha H. Sintering of acicular Fe2O3 powder. J Am Ceram Soc 1981;64. https://doi.org/10.1111/j.1151-2916.1981.tb09594.x.
[24] Patisson F, Mirgaux O, Birat J-P. Hydrogen steelmaking. Part 1: physical chemistry and process metallurgy. Matériaux Tech 2021;109:303. https://doi.org/10.1051/mattech/2021025.
[25] Ranzani da Costa A, Wagner D, Patisson F. Modelling a new, low CO2 emissions, hydrogen steelmaking process. J Clean Prod 2013;46:27–35. https://doi.org/10.1016/j.jclepro.2012.07.045.
[26] Hammam A, Li Y, Nie H, Zan L, Ding W, Ge Y, Li M, Omran M, Yu Y. Isothermal and non-isothermal reduction behaviors of iron ore compacts in pure hydrogen atmosphere and kinetic analysis. Min Metall Explor 2021;38:81–93. https://doi.org/10.1007/s42461-020-00317-3.
[27] Spreitzer D, Schenk J. Reduction of iron oxides with hydrogen—A review. Steel Res Int 2019;90. https://doi.org/10.1002/srin.201900108.
[28] Vyazovkin S, Burnham AK, Criado JM, Pérez-Maqueda LA, Popescu C, Sbirrazzuoli N. ICTAC kinetics committee recommendations for performing kinetic computations on thermal analysis data. Thermochim Acta 2011;520:1–19. https://doi.org/10.1016/j.tca.2011.03.034.
[29] Wang H, Liu B, Yang G, You C. Multistep kinetic study of Fe2O3 reduction by H2 based on isothermal thermogravimetric analysis data deconvolution. Int J Hydrogen Energy 2023;48:16601–13. https://doi.org/10.1016/j.ijhydene.2023.01.201.
[30] Piotrowski K, Mondal K, Wiltowski T, Dydo P, Rizeg G. Topochemical approach of kinetics of the reduction of hematite to wüstite. Chem Eng J 2007;131:73–82. https://doi.org/10.1016/j.cej.2006.12.024.
[31] Vyazovkin S, Burnham AK, Favergeon L, Koga N, Moukhina E, Pérez-Maqueda LA, Sbirrazzuoli N. ICTAC kinetics committee recommendations for analysis of multi-step kinetics. Thermochim Acta 2020;689:178597. https://doi.org/10.1016/j.tca.2020.178597.
[32] Moukhina E. Determination of kinetic mechanisms for reactions measured with thermoanalytical instruments. J Therm Anal Calorim 2012;109:1203–14. https://doi.org/10.1007/s10973-012-2406-3.
[33] Wendel J, Manchili SK, Hryha E, Nyborg L. Sintering behaviour of compacted water-atomised iron powder: effect of initial state and processing conditions.

Powder Metall 2020;63:338–48. https://doi.org/10.1080/00325899.2020.1833138.
[34] Gale WF, Totemeier T. Smithells metals reference book. eighth ed. 2004.
[35] Carpenter JA, Passaleva N, Häring M, Mikl G, Studart AR. 3D printing of hierarchical porous steel and iron-based materials. Adv Mater Technol 2023;8. https://doi.org/10.1002/admt.202200971.